High-resolution cryo-EM performance comparison of two latest-generation cryo electron microscopes on the human ribosome

Léo Frechin, Samuel Holvec, Ottilie von Loeffelholz, Isabelle Hazemann, Bruno Klaholz

▶ **To cite this version:**

Léo Frechin, Samuel Holvec, Ottilie von Loeffelholz, Isabelle Hazemann, Bruno Klaholz. High-resolution cryo-EM performance comparison of two latest-generation cryo electron microscopes on the human ribosome. Journal of Structural Biology, 2023, 215 (1), 10.1016/j.jsb.2022.107905 . hal-04076613

HAL Id: hal-04076613
https://hal.science/hal-04076613

Submitted on 20 Apr 2023

HAL is a multi-disciplinary open access archive for the deposit and dissemination of scientific research documents, whether they are published or not. The documents may come from teaching and research institutions in France or abroad, or from public or private research centers.

L'archive ouverte pluridisciplinaire **HAL**, est destinée au dépôt et à la diffusion de documents scientifiques de niveau recherche, publiés ou non, émanant des établissements d'enseignement et de recherche français ou étrangers, des laboratoires publics ou privés.

Journal of Structural Biology 215 (2023) 107905

Contents lists available at ScienceDirect

Journal of Structural Biology

journal homepage: www.elsevier.com/locate/yjsbi

Research Article

High-resolution cryo-EM performance comparison of two latest-generation cryo electron microscopes on the human ribosome

Léo Fréchin [1], Samuel Holvec [1], Ottilie von Loeffelholz, Isabelle Hazemann, Bruno P. Klaholz [*]

Centre for Integrative Biology (CBI), Department of Integrated Structural Biology, IGBMC (Institute of Genetics and of Molecular and Cellular Biology), 1 rue Laurent Fries, Illkirch, France
Centre National de la Recherche Scientifique (CNRS) UMR 7104, Illkirch, France
Institut National de la Santé et de la Recherche Médicale (Inserm) U964, Illkirch, France
Université de Strasbourg, Strasbourg, France

A B S T R A C T

Recent technological advances in cryo electron microscopy (cryo-EM) have led to new opportunities in the structural biology field. Here we benchmark the performance of two 300 kV latest-generation cryo electron microscopes, Titan Krios G4 from Thermofisher Scientific and CRYO ARM 300 from Jeol, with regards to achieving high resolution single particle reconstructions on a real case sample. We compare potentially limiting factors such as drift rates, astigmatism & coma aberrations and performance during image processing and show that both microscopes, while comprising rather different technical setups & parameter settings and equipped with different types of energy filters & cameras, achieve a resolution of around 2 Å on the human ribosome, a non-symmetric object which constitutes a key drug target. Astigmatism correction, CTF refinement and correction of higher order aberrations through refinement in separate optics groups helped to account for astigmatism/coma caused by beam tilting during multi-spot and multi-hole acquisition in neighbouring holes without stage movement. The obtained maps resolve Mg^{2+} ions, water molecules, inhibitors and side-chains including chemical modifications. The fact that both instruments can resolve such detailed features will greatly facilitate understanding molecular mechanisms of various targets and helps in cryo-EM structure based drug design. The methods and analysis tools used here will be useful also to characterize existing instruments and optimize data acquisition settings and are applicable broadly to other drug targets in structural biology.

1. Introduction

The contribution of single particle cryo electron microscopy (cryo-EM) to the structural biology field has been steadily increasing over the past decade, with a strong growth in the last few years as illustrated by the number of derived structures and atomic models that are deposited in the protein data bank (PDB) and electron microscopy data bank (EMDB), and specifically of large complexes which are more easily amendable to cryo-EM analysis than to X-ray crystallography (Fig. 1**A, B**). Of note, medium and high-resolution cryo-EM structures are all determined from data collected using electron microscopes operating under cryo conditions to preserve samples in a frozen-hydrated state. The proportion of high-resolution cryo-EM structures is increasing (Fig. 1**C**) and hence allows detailed insights into structures, their secondary structure and the position of the individual side-chains. This is important for a reliable derivation and validation of atomic models using various software (e.g. Phenix (Liebschner et al., 2019; Klaholz, 2019); Refmac (Murshudov et al., 2011), Buster (Smart et al., 2012) that allow detailed interpretation of the underlying molecular mechanisms, protein–protein or protein-RNA/DNA interactions, and inhibitor interactions within ligand binding pockets relevant for drug design. This impressive move of the cryo-EM field around the years 2013/2014 has become possible thanks to technological developments both on hardware and software sides, in particular since the introduction of direct electron detectors and CMOS (complementary metal-oxide semiconductor) cameras in ~ 2012/2013 (noticeable in the steep increase from 2013 onwards, Fig. 1**C**), which, combined with advanced image processing such as 2D & 3D classification methods to sort out different conformations and compositions of the structures (Klaholz et al., 2004; White et al., 2004; Penczek et al., 2006; Scheres et al., 2007; Elad et al., 2008; Simonetti et al., 2008; Klaholz, 2015) including focused classifications and refinements (von Loeffelholz et al., 2017; Huiskonen, 2018; Nakane et al., 2018), has allowed reaching resolution levels better than 3 Å (in total > 60% are resolved at better than 4 Å resolution, Fig. 1**C**). The high quality of experimental data and hence the primary performance of a transmission electron microscope in the first place is a *sine*

* Corresponding author at: Centre for Integrative Biology (CBI), Department of Integrated Structural Biology, IGBMC (Institute of Genetics and of Molecular and Cellular Biology), 1 rue Laurent Fries, Illkirch, France.
E-mail address: klaholz@igbmc.fr (B.P. Klaholz).
[1] Equal contribution.

https://doi.org/10.1016/j.jsb.2022.107905
Received 28 March 2022; Received in revised form 23 September 2022; Accepted 5 October 2022
Available online 12 October 2022
1047-8477/© 2022 The Authors. Published by Elsevier Inc. This is an open access article under the CC BY-NC-ND license (http://creativecommons.org/licenses/by-nc-nd/4.0/).

qua non requirement for resolving finest features in 3D structures, which are obtained from the recorded 2D projection images of the objects of interest. The ability and level of accuracy during image processing of i) identifying objects (particle selection), ii) centring and rotationally aligning particle images, and iii) determining their respective viewing (Euler) angles, depends in particular on a good signal over noise ratio, which in turn benefits from a good image contrast. Image processing methods such as 2D classifications based on multivariate statistical analysis (MSA) or maximum likelihood (ML) calculations can help to improve contrast through the combination of similar particle views into class averages, but the accuracy of such classifications yet again depends on the quality of the original experimentally collected data. Hence, obtaining well contrasted images while yet preserving high frequencies is crucial to be able to resolve fine details such as amino acid side-chains. A possibility is to acquire image data on an electron microscope equipped with contrast-increasing Volta phase plates (Cambie et al., 2007; Danev and Baumeister, 2016; Danev et al., 2017), which we have shown improve image processing parameters such as particle alignment and Euler angle assignment significantly (von Loeffelholz et al., 2018; von Loeffelholz and Klaholz, 2021). Another tool for noise reduction and contrast enhancement are energy filters that allow primarily recording the zero-loss electrons and thereby remove inelastically scattered electrons that otherwise contribute to noise, particularly at high spatial frequencies; this allows to obtain less "foggy" images that are easier to interpret and process.

To improve image data quality and enable effective image processing, major technological developments on high-end electron microscopes in biology have been introduced in the past 2 decades. These have focused on (i) gaining mechanical and thermal stability at low temperatures to obtain low drift rates (~1 Å / s) also when tilting during tomogram acquisitions, (ii) enabling transfer of multiple cryo-EM grids with automated upload and grid / cartridge fixation on the goniometer of the microscope, (iii) optimising the optical system to preserve parallel light conditions while working with different magnifications and settings (low dose, focus & expose modes etc.) along with automated data collection, (iv) improving the imaging system at different levels, such as the electron source (cold field emission gun [FEG]) with smaller energy spread and low divergence which improves beam coherence and brilliance, phase plates (installed at the back focal plane together with the objective aperture), possible Cs (spherical aberration) correctors, energy

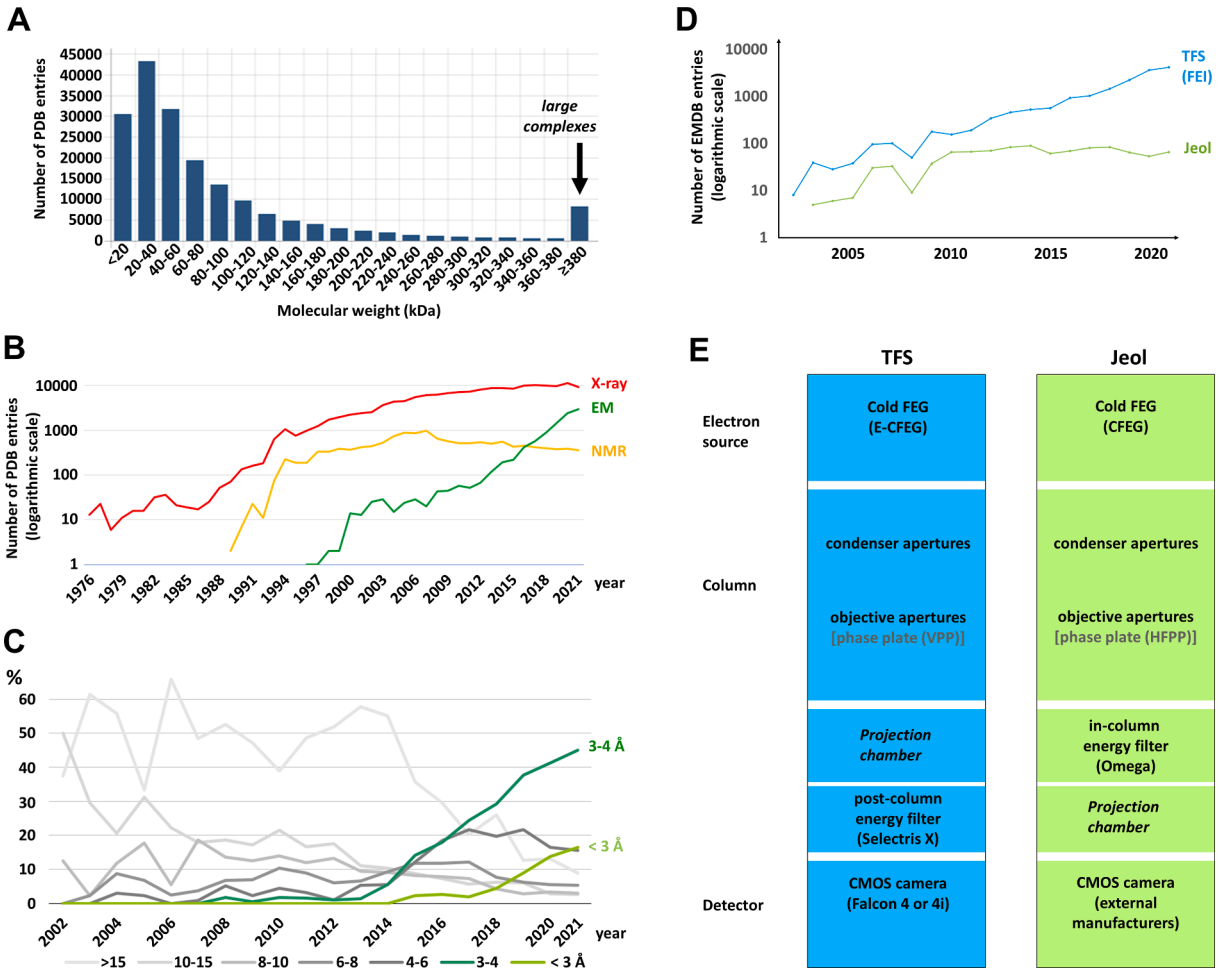

Fig. 1. The increasing contribution of cryo electron microscopy in the field of structural biology. (a) Number of protein data bank (PDB) entries to date plotted dependent on the molecular weight. **(b)** Number of PDB entries per year sorted by the method by which they were derived (orange: nuclear magnetic resonance; red: X-ray crystallography; green: electron microscopy; logarithmic scale). **(c)** Percentage of entries generated from cryo-EM data that were deposited between 2002 when the electron microscopy data bank (EMDB) started and now, sorted by the achieved resolution. EMDB entries generated with high-resolution cryo-EM structures are highlighted in light green (better than 3 Å resolution) and dark green (3–4 Å resolution range). **(d)** Number of cryo-EM maps deposited in the EMDB derived from cryo-EM data that were collected either with a cryo electron microscope from Jeol (green) or Thermo Fisher Scientific/FEI (blue); logarithmic scale. **(e)** Schematic representation of the high-end cryo electron microscopes produced by Thermo Fisher Scientific (Titan Krios G4) and Jeol (CRYO ARM 300) with cold field emission gun and energy filter as accessory options, which were used for the data presented in this article. Phase plates (indicated in grey) are available for these setups (positioned in the back focal plane) but were not used in this study.

filters, constant power lenses (higher beam coherence) and high-sensitivity cameras. Energy filters and CMOS cameras are often considered to be accessory pieces of equipment, but the so-called Omega filter on Jeol instruments has long been an integral part of the microscope. Only recently, Thermofisher Scientific (TFS, previously FEI and originally Philips) developed a post-column energy filter, the so-called Selectris; before, the usage of an energy filter on microscopes such as Polara or Titan Krios required a post-column installation from a different company, e.g. a Quantum Gatan Imaging Filter (GIF). In-column filters in principle have the advantage of reducing image distortions because the beam direction remains straight and they do not alter nominal magnification and work in any optical mode, while a post-column filter can in principle be installed/upgraded on any microscope. Energy filters have evolved to small energy spread values (e.g. slit range of 20 eV for GIF, 20 eV for Omega, and 10 eV for Selectris-X) and are recommended in particular for cellular analysis by tomography but may be also useful for single particle analysis. Finally, data collection from frozen-hydrated samples preserved in vitreous ice in order to reduce diffusion of free radicals and irradiation damage requires maintaining temperatures below the transition point from amorphous to crystalline ice (~-140 °C) (Lepault et al., 1983) during grid loading on the microscope and data collection when the sample is mounted on the goniometer of the microscope. This implies a series of practical and technical implementations on the microscopes for preserving low temperatures (typically below −165 °C) throughout the process of sample transfer & image acquisition to avoid devitrification and ice contamination and also maintain drift rates low during data collection by using appropriate insulation materials and constant cryogenic supply with liquid nitrogen. Hence, while the contribution to data banks from structures solved using image data from either TFS or Jeol microscopes is rather unequal (Fig. 1**D**), recent progress indicates that both companies provide similar tools (cold FEG, in/post-column energy filter etc., Fig. 1**E**). However, they have not been compared directly side-by-side yet with regards to performance, particularly considering that the integrated technologies are implemented rather differently.

Testing cryo electron microscopes is usually done with standard samples such as cross grating or oriented, micro-crystalline gold to test the optical system and maximum nominal resolution, and standard protein crystals to test isotropic magnification and calibrate magnification (catalase, tobacco mosaic virus etc.). In the vast majority of cases, simple test samples such as apo-ferritin or symmetric objects have been used (Bartesaghi et al., 2015; Nakane et al., 2020; Yip et al., 2020; Zhang et al., 2020) to check a microscope through a routine data collection run and estimate the resolution that can be reached in 3D reconstructions through image processing. Such test samples are easy to purify or obtain commercially and have the advantage of comprising internal symmetry of the object (octahedral (O) for apo-ferritin, D2 symmetry for β-galactosidase) which greatly favours image processing because high symmetries provide additional averaging and also help particle centring to allow quick feedback with relatively small data sets (e.g. 20–50 000 particles). However, these specimens are not fully representative of real case biological samples, which most often encompass no symmetry or comprise issues typical for macromolecular complexes such as compositional and conformational heterogeneity that require larger data sets to be addressed and hence longer data collections. Technical characteristics and data acquired from TFS and Jeol microscopes have been described individually (Hamaguchi et al., 2019; Merk et al., 2020; Fislage et al., 2020; Wu et al., 2020; Hamdi et al., 2020; Adachi et al., 2021; Efremov and Stroobants, 2021; Zhang et al., 2021; Kato et al., 2018; Maki-Yonekura et al., 2021), including also the 200 kV machines such as Glacios or Talos Arctica (TFS) and CRYO ARM 200 (Jeol), but no direct comparison has been done yet on the 300 kV high-end setups. In this work we analyse the performances of the two high-end cryo electron microscopes from TFS and Jeol, the Titan Krios and the CRYO ARM 300, both with the latest available options such as cold FEG emitter, post- or in-column energy filters, automated sample upload and automated data collection. As a test sample we used the human ribosome, a real case biological sample without internal symmetry of which we have determined the structure in the past (Khatter et al., 2015; Myasnikov et al., 2016; Natchiar et al., 2017; von Loeffelholz et al., 2017; von Loeffelholz et al., 2018; Wang et al., 2021). While the ribosome has become a sort of test sample for various image processing tools over the years, usually the bacterial ribosome is used for reasons of easy purification, stability and well-characterized conformational states, often further stabilized by bound factors and/or antibiotics to achieve higher resolution. By contrast, the human ribosome is much larger, has a more complex RNA and protein structural organisation, comprises more flexibility (e.g. on the 40S subunit head), and in the present study is not particularly stabilized in terms of conformation (no protein factors are added, the antibiotic used does not lock the human ribosome in a particular conformation etc.). The flexibility may impose some resolution limits but these would be similar for well-performing instruments because achieving high-resolution with a more flexible complex is only possible with good images & instruments and appropriate image processing. The usage of human ribosomes is therefore particularly appropriate to compare the performance of two instruments including on more challenging biological samples and closer to typical real case examples. In addition, it represents a key drug target for the development of new antibiotics and anticancer drugs directed against the human protein synthesis machinery (Myasnikov et al., 2016; Gilles et al., 2020). Benchmarking of the microscopes was done using test data of comparable size and processed in a similar manner, and key microscope and image processing parameters such as drift rates, image aberrations, Euler angle stability through refinements etc. were characterised. This comprehensive analysis of technologies provides a first direct comparison of two latest-generation electron microscopes that will be of particular interest to the structural biology community considering the exponentially growing contribution of cryo-EM in the field.

2. Results & discussion

Two cryo transmission electron microscopes were used for the present benchmarking, the Titan Krios G4 (TFS) and the CRYO ARM 300 (Jeol), both equipped with energy filters (Selectris-X and Omega, respectively, see scheme in Fig. 1**E**) and two high-end direct electron detector cameras operating in counting mode to measure individual electron events, the Falcon 4 and Gatan K3 for the TFS and Jeol microscopes respectively, where the Falcon 4 (TFS) is integrated in the system comprising a Selectris X energy filter. Both instruments were operated at an acceleration voltage of 300 kV, and both contained a cold FEG source, called E-CFEG (TFS) or CFEG (Jeol). An automatic liquid nitrogen filling system minimizes personal intervention and facilitates continuous data collection. Automated upload of the cryo-EM grids is done by a cryogenic sample manipulation robot called “autoloader” (TFS) or “automated cryo-transfer system” (Jeol), into which a small dewar with the pre-mounted specimen grids is introduced. Human 80S ribosome sample grids were prepared according to our previously published procedures (Khatter et al., 2014; Khatter et al., 2015; Myasnikov et al., 2016; Natchiar et al., 2017) (see methods) and sent in a dry shipper for data collection at the TFS factory in Eindhoven and at the RIKEN Osaka cryo-EM facility proposed by Jeol (giving rise to data sets 1 and 2, respectively, as named in the following). The microscopes were aligned for parallel beam conditions using coma free alignment procedures and data were collected in automated manner with either the EPU software (TFS) or the academic software SerialEM (Mastronarde, 2003) installed on the computer operating the Jeol instrument (see methods). Köhler illumination (Köhler, 1893) was used to remove interference fringes (called fringe-free imaging or zero fringe system by TFS or Jeol, respectively) to facilitate collecting several images per hole (multi-spot or “multi-shot”). Beam tilt compensation (Jeol) or aberration free image shift (AFIS, TFS; beam-image shifts combined with off-axis coma and astigmatism correction) were used to allow acquisitions on

Table 1

Instrumentation & data acquisition	Data set 1	Data set 2
Microscope	Titan Krios G4	CRYO ARM 300
Electron source	E-CFEG	CFEG
Energy filter	Selectris X	Omega
Slit width (eV)	10	20
Non-isochromaticity (eV)	< 0.3	< 0.35
Acceleration voltage (kV)	300	300
*C*2 condenser aperture (μm)	50	50
Objective aperture	-	-
CMOS camera	Falcon 4	Gatan K3
Physical pixel size (μm)	14	5
Image format / mode	EER	CDS
Nominal magnification	165 000	60 000
Field of view (Å^2)	8.7×10^6	15.9×10^6
Automation software	EPU	SerialEM
Pixel size (Å)	0.72 (0.36 super-res)	0.82 (0.41 super-res)
Nominal defocus range (μm)	−0.5 to −1.1	−1.0 to −2.0
Number of micrographs used	13,624	4,580
Number of images per hole	3	4
Beam diameters (μm)	0.65	1.1
Waiting time after stage movement/before first picture (s)	20 (before focusing)	10 (during focusing)
Exposures per stage position	~8 × 3 = ~24	9 × 4 = 36
Data collection speed	309 images / h (~3x3 multiple holes)	400–500 images / h (3x3 multiple holes)
Total electron dose (e-/Å^2)	30	40
Exposure time (s)	3.58	3.0
Fraction dose (e-/Å^2)	1	1

several neighbouring holes without stage movement (multi-hole). These acquisition modes (Cheng et al., 2018; Weis and Hagen, 2020) help maintaining mechanical stability & low drift rates and increase data collection speed. Considering that the cameras used have rather different physical pixel sizes the magnification was chosen such that a similar pixel size on the specimen was obtained and fine enough to enable high-resolution structural analysis (0.72 and 0.82 Å / pixel for data sets 1 and 2, giving a Nyquist frequency of 1.4 and 1.6 Å, respectively). The specific devices and parameter settings used for data collection are summarized in Table 1.

The two data acquisitions gave good images with similar contrast with the Selectris X and Omega energy filters when compared at the same defocus (Fig. 2**A**). High resolution information is present as judged from the power spectra in which Thon rings are visible up to a resolution range of 2.3–2.5 Å (Fig. 2**B**). Data collection speed is comparable for the 2 acquisitions with about 300–400 images per hour. This could potentially be increased by more extensive multi-hole acquisitions but may become also limited at some point by the data acquisition speed of the cameras and reduced stabilisation after stage shift. Acquisition speed can vary significantly depending on settings used, in particular whether multi-spot, AFIS etc. are used or not; e.g. reducing the beam size (diameter) is beneficial for multi-spot data collection strategies (data set 1 and 2 for the TFS and Jeol microscopes have 0.65 μm and 1.1 μm, respectively, the latter could be further reduced). Finally, the usage of a cold FEG regularly required a so-called "flashing" of the tip to clean the emitter during which the acquisition is stalled; as this procedure is integrated into the data collection workflow it did not disturb data collection significantly and does not seem to influence data quality in a noticeable manner because beam alignments are preserved; the decreasing beam intensity between flashing events (Suppl. Fig. 1) is accounted for by normalization of the images during data processing, but not during dose weighting in motion correction / movie processing or particle polishing tasks, which work with a constant electron dose per frame (hence, images acquired towards the end of a flashing cycle would get low-pass filtered more strongly).

Image processing of data sets 1 and 2 was done with comparable particle numbers and using the same procedures and software (see methods), with the exception that the two cameras used gave rise to image data of variable nature (EER or CDS) and in different formats that needed to be processed differently (see methods). Drift rates per micrograph are larger and fluctuate more for data set 2 (Jeol; median values of drift are 2.3 and 5 Å / s, respectively; Fig. 2**C**). Data set 1 (TFS) required using more micrographs to compensate for the slightly lower particle concentration on the cryo-EM grid and the smaller field of view (considering that camera areas and pixel sizes are different; Table 1), but the estimated resolution on the micrographs is similar (Fig. 2**D**). Image processing performed overall well with similar characteristics such as Euler angle precision from early iterations on (angular distribution of particles is similar, Suppl. Fig. 2), number of iterations required, refinement stability of Euler angles over iteration cycles (Fig. 2**E,F**). It provided similarly resolved structures of the human ribosome, the final resolution values being in the 2.1–2.2 Å resolution range (Fig. 2**G**). We used relatively large particle box sizes during image processing (640 pixels, particle diameter would correspond to 440 pixels) to avoid delocalization of higher resolution Fourier component outside the images (even larger box sizes did not improve resolution in our hands). We also applied anisotropic magnification correction (Glaeser et al., 2021), CTF refinement, correction of higher order aberrations (Zivanov et al., 2018) and Bayesian polishing (Fig. 2**G;** additional CTF refinement in a final round did not improve resolution further). The obtained resolution of the reconstructions was plotted against the amount of particles used to represent a linear dependence (Rosenthal and Henderson, 2003) (Fig. 2**H**) as calculated from random subsets of each dataset and using independent full 3D refinements (see methods). The plot shows excellent B-factor values in the 30 Å^2 range, with slightly better values for data set 1 but this does not translate to noticeable differences in the two cryo-EM maps.

However, more detailed analysis of refinement parameters during image processing revealed that the data sets have rather different characteristics: (i) data set 2 (Jeol microscope) exhibited significantly higher astigmatism values (e.g. ~ 71 nm for data set 2 as compared to ~ 9 nm for data set 1, TFS microscope), (ii) data set 2 required a larger amount of anisotropic magnification correction (0.34% versus 0.007% for data set 1), and (iii) the data sets comprised a different defocus distribution range, the second being larger and extending to higher defocus values (see plots in Fig. 3**A,B**). This prompted us to split the particle data set into lower and higher defocus parts (95 k and 134 k particles, respectively) and refine each subset separately. The resulting maps have the same resolution (2.4 Å), behaving like the half subsets used for the B-factor plot with regards to the reduced number of particles that impairs resolution (Fig. 2**H**). The comparable resolution reached for both defocus subsets indicates that the higher defocus data set does not suffer from a resolution drop even though the CTF envelope function could be expected to dampen the high-frequency amplitudes in the power spectra. This is consistent with the fact that a cold FEG provides an increased envelope function at high spatial frequencies at higher underfocus (Hamaguchi et al., 2019).

Finally, we noticed differing properties of the two data sets with regards to astigmatism, and as it turns out, beam tilt / coma (Fig. 3**C-G**). While data set 1 (TFS microscope) has a narrow distribution of astigmatism values irrespective of the spot position (between 0 and 20 nm), data set 2 (Jeol microscope) shows a series of peaks (with values of ~ 20 nm width but covering a full range between 0 and +/-170 nm). As these are relatively narrow distributions it is possible that the high values originate from the data collection procedure in which multi-hole acquisitions are achieved by beam tilting, *i.e.* this is in fact off axis coma, which results in a phase error that can affect high spatial frequencies (Glaeser et al., 2011; Zivanov et al., 2018). On the specific electron microscope used, astigmatism and beam tilting appear not corrected optimally (Fig. 3**C-G**) even though a coma compensation procedure was used according to the manufacturer; specifically, refinement of the parameters for neighbouring holes reveals astigmatism and beam tilt as illustrated by refinement in separate optics groups (Zivanov et al., 2020)

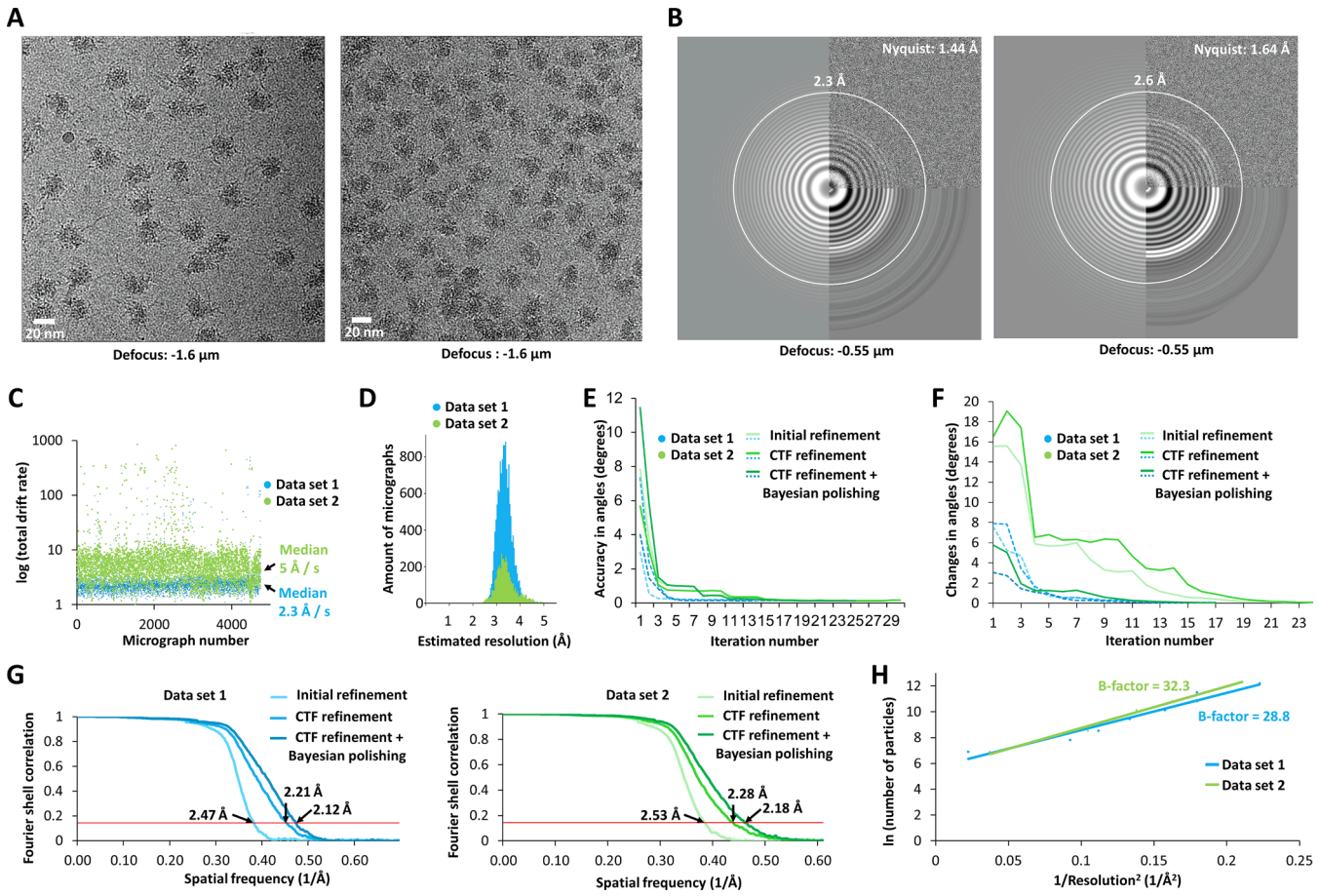

Fig. 2. Typical features of the electron microscopes as revealed by image processing and a series of analysis tools. (a) Field of human 80S ribosome particles from data sets 1 and 2 (TFS & Jeol, left and right, respectively). **(b)** Powerspectra from data sets 1 and 2 (left and right, respectively) with theoretical CTF (left), experimental CTF (top right), and CTF obtained by equiphase averaging (bottom-right). The estimated maximum resolution is indicated by a white ring. **(c)** Plot of the total drift rate per micrograph (Å / s) displayed at logarithmic scale (median values are indicated; the comparison uses only the first 4758 micrographs which is the same number used for data set 2; data sets 1 (TFS) and 2 (Jeol) in blue and green, respectively, according to the colour code in Fig. 1**e**). **(d)** Estimated resolution of micrographs for data sets 1 and 2; data set 1 comprised more data to compensate for the lower particle concentration (see panel **a**). **(e)** Estimated accuracy of Euler angle attribution during 3D refinement for data sets 1 and 2 at various steps of refinement. **(f)** Changes on Euler angle attributions occurring during 3D refinement for data sets 1 and 2 at various steps of refinement. **(g)** Fourier shell correlation (FSC) curves for data sets 1 (left) and 2 (right) at various steps of refinement (post-processing before CTF refinement (initial refinement), after CTF refinement cycles including anisotropic magnification, beam tilt and trefoil aberrations, 4th order aberrations, defocus per-particle and astigmatism per-micrograph correction (CTF refinement) and after Bayesian polishing (CTF refinement + Bayesian polishing). Resolution is estimated at $FSC_{0.143}$ (values labelled with arrows). **(h)** Plot of ln(number of particles) = f(1/Resolution^2) for data sets 1 and 2 obtained after 3D refinements with sub-half particle sets. B factors of each data set correspond to the slope obtained from the linear fit.

(Fig. 3**D-G**; interestingly, astigmatism and beam tilt parameters appear unrelated in the data: compare panels **D** and **F**, e.g. the central hole (#1) has virtually no astigmatism but significant beam tilt; the off-set in panel **F** points to sub-optimal, non-coaxial beam alignment, combined with astigmatism visible in panel **D**). By contrast, data set 1 shows that residual astigmatism and coma have been corrected to a large extent (Fig. 3**C**; further analysis of individual optics groups for a given stage position appeared therefore not necessary and was also not possible due to the irregular pattern of AFIS data collection; see methods). All images in data set 1 were treated as one optics group because there were very little aberrations after AFIS correction, while for data set 2 aberrations were estimated per-hole (see methods). The early astigmatism correction, CTF refinement and correction of higher order aberrations during image processing (Zivanov et al., 2018) of data set 2 (Fig. 3**D-G**; see methods) was able to account for the astigmatism/coma issues and still allowed reaching high resolution. It could be useful to have coma correction done in more detail when performing multi-hole data collections, which would make it also more robust with regards to processing with different software.

The cryo-EM maps obtained from data sets 1 and 2 show features typical of a 2 Å structure (Fig. 4). The details on the amino acid side chains and RNA nucleotides (Fig. 4**A,B**) are better than our previous data on the human ribosome (Natchiar et al., 2017) (obtained with an earlier Titan Krios microscope and a Falcon 2 camera, see comparison in methods section). Many regions of the maps reveal ~ 2 Å resolution according to local resolution analysis, resolving details on the chemical modifications of the ribosomal RNA (Fig. 4). For example, the amino group of Am2363 and amino and keto groups of Gm2364 & Gm2365 and their 2′-O methyl groups can be distinguished better than before (Natchiar et al., 2017; Wang et al., 2021) (Fig. 4). Mg^{2+} ions with their associated individual water molecules are resolved and a bound ligand is clearly visible (Fig. 4**A,B**; present in the sample used for data set 2, absent for data set 1 for comparative purposes). Reaching such resolution levels on complex macromolecular assemblies, in particular without internal symmetry, is an important achievement and will greatly facilitate understanding molecular mechanisms. It underlines the strength of such approaches for cryo-EM based drug design which will be applicable for many other drug targets.

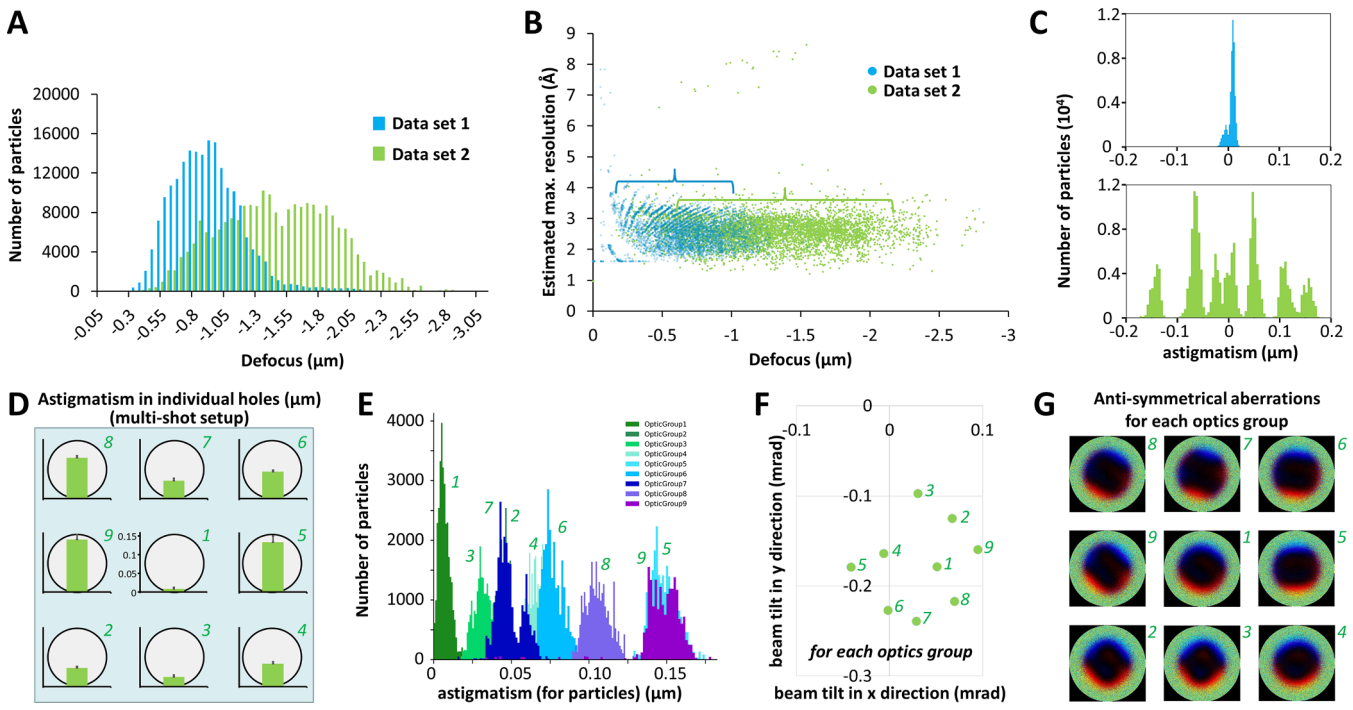

Fig. 3. Analysis of defocus distributions and astigmatism / beam tilt / off-axis coma. (a) Distribution of defocus values for particles from data sets 1 and 2 (TFS and Jeol microscopes, respectively). **(b)** Distribution of the estimated maximum resolution per micrograph relative to their defocus for data sets 1 and 2 (first 4758 micrographs as in panel c) as estimated with the Gctf software. **(c)** Histograms of the particle distribution relative to their astigmatism (in fact off-axis coma) for data sets 1 and 2 (top and bottom, respectively, first 4758 micrographs as in panels c and i) as estimated with the Gctf software. **(d)** Average astigmatism of particles relative to the image acquisition on a given stage position on the sample during the multi-hole acquisition for the data set 2 (schematic representation of the 9 grid holes in the background). **(e)** Distribution of astigmatism over the 9 spots according to the optics groups (data set 2). **(f)** Distribution of beam tilt values in x and y direction over the 9 spots for each optics groups. **(g)** anti-symmetrical plots for the 9 spots of the optics groups revealing beam tilt / off-axis coma according to high-order aberration estimation with the software Relion (Zivanov et al., 2020).

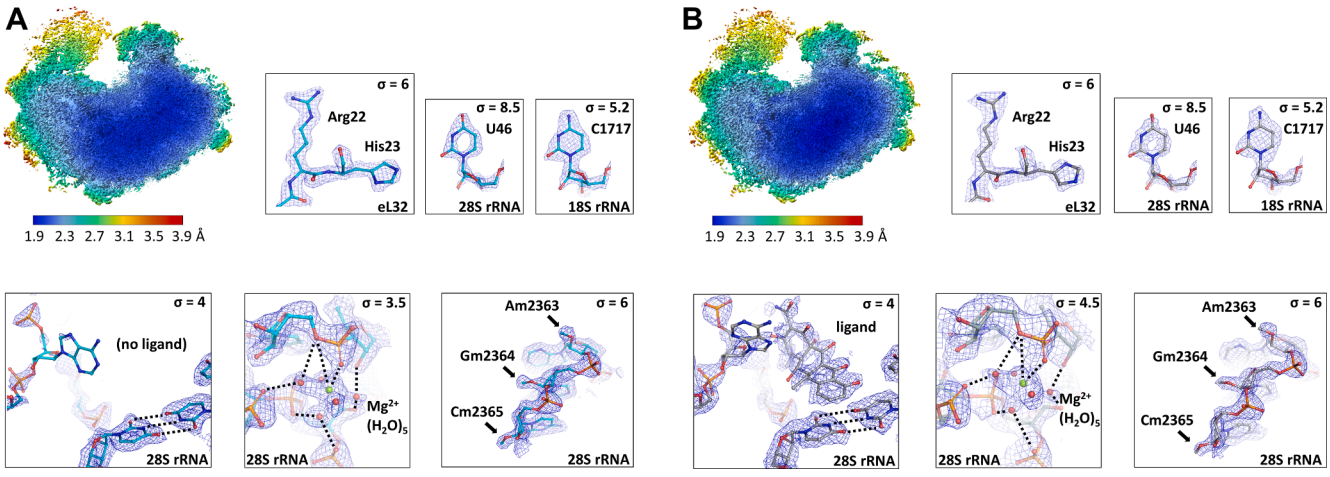

Fig. 4. High-resolution features in the cryo-EM maps obtained for the human ribosome. (a, b) panels describe data sets 1 and 2 (TFS and Jeol microscopes), respectively. Top left: local resolution estimated with Relion; other panels show detailed features of the cryo-EM maps (sigma level indicated in top right corners): region of ribosomal protein eL32, U46 in the 28S rRNA, C1717 in the 18S rRNA, an inhibitor binding pocket in absence and presence of the ligand (Watson-Crick base pairing shown with dashed lines), hydrated Mg^{2+} ion with associated water molecules and their hydrogen bonding with neighbouring residues (indicated with dashed lines), example of chemical modifications in a base triplet with 2′-O methylations in the 28S rRNA.

Taken together, while the implemented engineering technologies and specific settings of the TFS and Jeol systems are rather distinct, the present benchmarking results show that overall similar results can be obtained. Nevertheless, specific data characteristics such as coma, anisotropic magnifications etc. required more advanced image processing procedures (not necessarily available in all software) to provide high-resolution information to a similar level. For routine usage, including for projects with different sample types and variable quality (homogeneity, particle distribution etc.), robust and easy-to-use equipment and software interfaces are an advantage. A practical issue to also consider for microscope installations are the room specifications, e.g. the required ceiling height (3.04 m for a Titan Krios G4 and 3.85 m for a CRYO ARM 300). Regarding sample handling, both systems provide up to 12 specimen slots, but in the Jeol version only 4 grids can be mounted

at once, hence 3 transfers are required for uploading 12 specimens. This also points to the issue of compatibility between instruments, e.g. sample transfer between Jeol JEM FSC and CRYO ARM series requires unclipping the grid, between Glacios and Titan Krios the same sample holding dewar can be used, and between Jeol and TFS instruments the grids can be transferred but this requires physically removing and relocating the grid from one holder to another (though no unclipping is needed if "autogrids" are used in the Jeol cartridge), which increases the risks of grid loss and contaminations and hampers the workflow and speed of sample handling. To avoid the associated throughput reduction of sample screening and data collection future developments will be needed to facilitate sample optimisation & testing on medium-end instruments before physically moving samples to a high-end cryo electron microscope for high-resolution data collection. Furthermore, microscopes need to be made better compatible for various direct electron detectors at the level of integration and operation with software considering that CMOS cameras are evolving at high pace; the present data also suggest that the Gatan K3 and Falcon 4 cameras provide similar performances in achieving high-resolution.

The methods and analysis tools used here will be applicable broadly to other biological samples and cryo-EM data collections/processing, including on existing instruments to characterize microscopes and optimize data acquisition settings. This comprehensive comparative analysis of two high-end instruments and their performances will be of key importance for the structural biology field to further extend the exciting potential of cryo-EM.

3. Material and Methods

3.1. Sample preparation

Human 80S ribosomes were purified from HeLa cells for both data sets following our previously established procedures (Khatter et al., 2014; Khatter et al., 2015; Myasnikov et al., 2016; Natchiar et al., 2017). After resuspension in buffer A (100 mM KOAc, 5 mM $Mg(OAc)_2$, 20 mM sodium cacodylate) for data set 1 and in buffer B (100 mM KCl, 5 mM $Mg(OAc)_2$, 20 mM HEPES pH 7.6, 1 mM DTT) for data set 2, both samples were diluted to a concentration of ~1-2 mg/mL (0.24-0.48 μM) into their respective buffers. For data set 2 an antibiotic was added to a final concentration of 1 mM and the sample was incubated 5 minutes at 37°C and kept at room temperature until grid preparation. Both samples were then applied to holey R 2/2 carbon 300 mesh rhodium plated copper grids (Quantifoil) coated with a thin carbon film and treated with a plasma-cleaner (Fischione; 90% Argon, 10% oxygen), then blotted and cryo cooled into liquid ethane using a Vitrobot IV (Thermo Fisher Scientific, The Netherlands) with the chamber operating at 100% humidity and at 10°C for dataset 1 or 17°C for dataset 2.

3.2. Cryo-EM data collection

Cryo-EM grids were sent in a dry shipper and test data were collected at the TFS factory in Eindhoven for data set 1 and at the RIKEN Osaka cryo-EM facility for data set 2. For data set 1, data acquisition was done with the software EPU2 (Thermofisher Scientific) on a Titan Krios G4 electron microscope equipped with an E-CFEG electron source, a post-column mounted Selectris X energy filter and a Falcon 4 camera operating in electron event representation (EER) mode (Guo et al., 2020). With the Selectris energy filter the microscope needs to be operated in EFTEM (energy filtered transmission electron microscopy) mode, similarly to the settings for a K3 camera; the difference is that the path length is smaller for the Selectris and the change in nominal magnification is only about 10% (see Table 1 regarding the effective field of view). 13624 movies were acquired in a fringe-free setup with 3 shots per hole acquiring multiple holes (in best conditions up to 9, here ~8, no regular pattern used in the AFIS/EPU procedure) per stage position by using AFIS (image shift of 6 μm) with a waiting time of 20 s after each stage shift (before focusing starts) and an acquisition rate of 309 images / h. The acquisition was done in super-resolution mode with a pixel size of 0.36 Å / pixel (165 000 x magnification) and a total dose equivalent to 30 e^- / $Å^2$ in 861 EER frames in 3.58 seconds with a target defocus range of -0.5 to -1.1 μm with increment steps of 0.2 μm (see Table 1). For comparison, our previous study a few years earlier (Natchiar et al., 2017) comprised a different generation setup: Titan Krios G1, S-FEG, 300 kV, no energy filter, Falcon II camera; settings: data collection with EPU, magnification 77 778, pixel size 0.85 Å, defocus range -0.4 to -2.5 μm, 6528 micrographs, 1 exposure per stage position, total dose 60 e-/$Å^2$, 1 s exposure time, fraction dose 3.5 e-/$Å^2$.

For data set 2, data acquisition was done with the SerialEM software[41] on the Jeol CRYO ARM 300 at the RIKEN centre of the Osaka University equipped with a CFEG electron source, an Omega energy filter and a Gatan K3 camera operating in correlated double sampling (CDS) mode (Sun et al., 2021). 4580 movies were acquired in a fringe-free setup with 4 shots per hole acquiring multiple holes (3x3 per stage position) using beam-image shift (Cheng et al., 2018) (aberration free image shift, 7 μm) with a waiting time of 10 seconds after each stage shift (during focusing) at an acquisition rate of 400-500 images / hour. The acquisition was done in super resolution mode with a pixel size of 0.41Å / pixel (60 000 x magnification) and a total dose of 40 e^-/ $Å^2$ fractionated into 40 frames over 3.0 seconds with a target defocus range of -1.0 to -2.0 μm (see Table 1). Less micrographs were required thanks to the higher particle concentration on the cryo-EM grid and the larger field of view (calculated according to (4096 pixels x 0.72 Å/pixel) (Klaholz, 2019) for the Falcon 4 camera (data set 1) and (5760 pixels x 0.82 Å/pixel) x (4092 pixels x 0.82 Å/pixel) for the K3 camera (data set 2; see Table 1).

Regarding recommended dose rates, these are comparable for the two CMOS cameras used: for the K3 camera in CDS mode it is 8-10 e-/($Å^2$*s) and for the Falcon 4 it is 5-10 e-/($Å^2$*s). Here a dose rate of 13 and 8 e-/($Å^2$*s) was used for the K3 and Falcon 4 cameras, respectively.

3.3. Cryo-EM data processing

Data pre-processing of both data sets was done with Relion (Zivanov et al., 2018). In the case of data set 1 (TFS microscope) the EER frames were regrouped into 30 frames. To get a dose equivalent to 30e^- / $Å^2$ over 30 frames, every 28 frames were grouped as one dose fraction, ignoring the last 21 higher dose frames. First, Relion's motion correction algorithm (Zivanov et al., 2018) was applied on the frames to generate micrographs, which included dose weighting as part of the movie alignment. During this step data set 1 was coarsened to 0.72 Å / pixel while data set 2 (Jeol microscope) was kept at the original pixel size of 0.72 Å / pixel. CTF estimation was done using Gctf (Zhang, 2016) inside Relion (Zivanov et al., 2018) using a Cs value of 2.7 mm using equiphase averaging (EPA) (Zhang, 2016). Particle picking was done with crYOLO (Wagner et al., 2019). 2D and 3D classifications, 3D refinements, map sharpening, CTF refinement, Bayesian polishing and local resolution estimation were done using Relion v3.1.3 (Zivanov et al., 2018) using the implementation of ResMap (Kucukelbir et al., 2014). After particle picking, 634 158 particle positions were selected for data set 1 (see Table 2). Particles were extracted 8 times coarsened with a box-size of 80 pixels. Particles were classified into 50 2D classes, resulting in 220

Table 2

Image processing	Data set 1	Data set 2
Total number of extracted particles	634,158	484,393
Final number of particles used	199,371	229,233
Box size (pixels)	640	512
Symmetry	C1	C1
Map sharpening B-factor ($Å^2$)	−37.30	−41.11
Global map resolution (Å)	2.12	2.18

The authors declare no competing financial interests.

889 particles kept for further processing. Particles were re-extracted with a pixel size of 1.44 Å / pixel (2 times coarsened) and used as an input for 3D refinement using as reference the map of our previous human ribosome structure (Natchiar et al., 2017) low-pass filtered to 60 Å. The resulting 3 Å resolution map was used as reference for a 3D global classification into 4 classes without alignment. 199371 particles from the main class (~90% of the total particles) were selected and particles were extracted in the original pixel size with a box-size of 640 pixels followed by a 3D refinement, resulting in a 2.47 Å resolution map. Cycles of CTF refinement and 3D refinement were done to first correct 4th order aberrations, second beam tilt and trefoil aberrations, per-particle defocus and per-micrograph astigmatism, and finally anisotropic magnification. After further 3D refinement a map at 2.21 Å resolution was obtained. Bayesian polishing was applied on particles, followed by a 3D refinement and map sharpening (postprocessing) using a B factor filtering of -37.30 Å^2, resulting in a 2.12 Å resolution map. The final postprocessing step used a mask derived from the 3D refinement map applying a 15 Å lowpass filter, extended by 3 pixels and with a soft edge of 9 pixels.

Regarding data set 2, 484 393 particle positions were selected after particle picking, for data set 2 (see Table 2). Particles were then extracted 2 times coarsened with a box-size of 256 pixels. Particles were classified with 2D classification into 50 2D classes, resulting in 303 401 particles used for an *ab initio* 3D reconstruction that was used as a reference for a 3D global classification into 4 classes. 229 233 particles from the 3 best classes were selected for a 3D refinement using as reference the map of the main class obtained by the previous 3D classification step, resulting in a 3.3 Å resolution map. Particles were extracted in the original pixel size of 0.82 Å / pixel with a box size of 512 pixels and 3D refinement resulted in a 2.53 Å resolution map. Cycles of CTF refinement and 3D refinement were done to correct first anisotropic magnification, second 4th order aberrations, beam tilt and trefoil aberrations, and finally per-particle defocus and per-micrograph astigmatism. The subsequent 3D refinement resulted in a 2.28 Å resolution map. Bayesian polishing was performed on the particles, followed by a 3D refinement and map sharpening (postprocessing) using a B factor filtering of -41.11 Å^2, resulting in a 2.18 Å resolution map. Postprocessing was done using a mask obtained from 3D refinement map applying a 15 Å lowpass filter, extending the map by 3 pixels and applying a soft edge of 9 pixels.

Further analysis of individual optics groups was not possible for data set 1 due to the irregular pattern of AFIS / EPU data collection which selects neighbouring holes in a non-consecutive manner (also not evident from the image file names); hence, all images in data set 1 were treated as one optics group because there are very little aberrations (thanks to AFIS correction which comprises beam-image shifts combined with off-axis coma and astigmatism correction), while for data set 2 aberrations were estimated per-hole (grouping the 4 shots per hole) to account for the aberrations during image processing.

Half subsets of the data were extracted randomly and refined independently. The obtained resolution of the 3D reconstructions was plotted against the amount of particles (Rosenthal and Henderson, 2003) using the formula ln (number of particles) against 1 / (obtained resolution) (Klaholz, 2019). A linear fit line for each dataset was plotted in Excel; the B-factors were calculated as 2 x the slope of each curve. Resolution estimation by Fourier shell correlation (FSC) (Rosenthal and Henderson, 2003; van Heel and Schatz, 2005) calculations (0.143 criterion) were done in Relion (Zivanov et al., 2018) using half maps. Map interpretation was done by docking the atomic model of the 80S human ribosome (PDB ID 6QZP) (Wang et al., 2021)into the final maps followed by an automated rigid body fit in Chimera (Pettersen et al., 2004) and subsequent refinements including manual rebuilding in Coot (Emsley et al., 2010) and real space refinement in Phenix1, (Afonine et al., 2018). Figures were prepared using ChimeraX 1.2.5 (Pettersen et al., 2021) and Pymol (DeLano, 2002).

Declaration of Competing Interest

The authors declare that they have no known competing financial interests or personal relationships that could have appeared to influence the work reported in this paper.

Data availability

Data will be made available on reasonable request.

Acknowledgement

We thank the TFS and Jeol companies for kindly making their microscope setups available for test data collection, which was performed by Evgeniya Pechnikova (TFS, Eindhoven, NL) and Fumiaki Makino (on behalf of Jeol, Osaka, Japan). We acknowledge Jonathan Michalon, Mathieu Schaeffer and Nicolas Ballet for IT support. This work was supported by CNRS, Association pour la Recherche sur le Cancer (ARC), Institut National du Cancer (INCa_16099), the Fondation pour la Recherche Médicale (FRM), Ligue nationale contre le cancer (Ligue) and Agence Nationale pour la Recherche (ANR) and USIAS of the University of Strasbourg (USIAS-2018-012). This work of the Interdisciplinary Thematic Institute IMCBio, as part of the ITI 2021-2028 program of the University of Strasbourg, CNRS and Inserm, was supported by IdEx Unistra (ANR-10-IDEX-0002), and by SFRI-STRAT'US project (ANR 20-SFRI-0012) and EUR IMCBio (ANR-17-EURE-0023) under the framework of the France 2030 Investment Program. The electron microscope facility was supported by the Alsace Region and by the French Infrastructure for Integrated Structural Biology (FRISBI) ANR-10-INSB-05-01 under the France 2030 Program, by the epiRNA grant (Fonds Régional de Coopération, Région Grand Est; Compétitivité Alsace 2014-2020, FEDER), by Instruct-ULTRA, Instruct-ERIC and iNEXT-Discovery.

We thank the referees for their useful suggestions.

Appendix A. Supplementary data

Supplementary data to this article can be found online at https://doi.org/10.1016/j.jsb.2022.107905.

References

Adachi, N., et al., 2021. 2.85 and 2.99 Å resolution structures of 110 kDa nitrite reductase determined by 200 kV cryogenic electron microscopy. J. Struct. Biol. 213, 107768.
Afonine, P.V., et al., 2018. New tools for the analysis and validation of cryo-EM maps and atomic models. Acta Crystallogr. Sect. Struct. Biol. 74, 814–840.
Bartesaghi, A., et al., 2015. 2.2 Å resolution cryo-EM structure of β-galactosidase in complex with a cell-permeant inhibitor. Science 348, 1147–1151.
Cambie, R., Downing, K.H., Typke, D., Glaeser, R.M., Jin, J., 2007. Design of a microfabricated, two-electrode phase-contrast element suitable for electron microscopy. Ultramicroscopy 107, 329–339.
Cheng, A., et al., 2018. High resolution single particle cryo-electron microscopy using beam-image shift. J. Struct. Biol. 204, 270–275.
Danev, R., Baumeister, W., 2016. Cryo-EM single particle analysis with the Volta phase plate. eLife 5. https://doi.org/10.7554/eLife.13046.
Danev, R., Tegunov, D., Baumeister, W., 2017. Using the Volta phase plate with defocus for cryo-EM single particle analysis. eLife 6. https://doi.org/10.7554/eLife.23006.
DeLano, W., 2002. PyMOL 0.99.
Efremov, R.G., Stroobants, A., 2021. Coma-corrected rapid single-particle cryo-EM data collection on the CRYO ARM 300. Acta Crystallogr. Sect. Struct. Biol. 77, 555–564.
Elad, N., Clare, D.K., Saibil, H.R., Orlova, E.V., 2008. Detection and separation of heterogeneity in molecular complexes by statistical analysis of their two-dimensional projections. J. Struct. Biol. 162, 108–120.
Emsley, P., Lohkamp, B., Scott, W.G., Cowtan, K., 2010. Features and development of Coot. Acta Crystallogr. D Biol. Crystallogr. 66, 486–501.
Fislage, M., Shkumatov, A.V., Stroobants, A., Efremov, R.G., 2020. Assessing the JEOL CRYO ARM 300 for high-throughput automated single-particle cryo-EM in a multiuser environment. IUCrJ 7, 707–718.
Gilles, A., et al., 2020. Targeting the Human 80S Ribosome in Cancer: From Structure to Function and Drug Design for Innovative Adjuvant Therapeutic Strategies. Cells 9, E629.
Glaeser, R.M., et al., 2021. Defocus-dependent Thon-ring fading. Ultramicroscopy 222, 113213.

Glaeser, R.M., Typke, D., Tiemeijer, P.C., Pulokas, J., Cheng, A., 2011. Precise beam-tilt alignment and collimation are required to minimize the phase error associated with coma in high-resolution cryo-EM. J. Struct. Biol. 174, 1–10.
Guo, H., et al., 2020. Electron-event representation data enable efficient cryoEM file storage with full preservation of spatial and temporal resolution. IUCrJ 7, 860–869.
Hamaguchi, T., et al., 2019. A new cryo-EM system for single particle analysis. J. Struct. Biol. 207, 40–48.
Hamdi, F., et al., 2020. 2.7 Å cryo-EM structure of vitrified M. musculus H-chain apoferritin from a compact 200 keV cryo-microscope. PloS One 15, e0232540.
Huiskonen, J.T., 2018. Image processing for cryogenic transmission electron microscopy of symmetry-mismatched complexes. Biosci. Rep. 38, BSR20170203 https://doi.org/10.1042/BSR20170203.
Kato, T., Terahara, N., Namba, K., 2018. Electron Microscopy Data Bank. Electron Microscopy Data Bank. https://www.ebi.ac.uk/emdb/EMD-6840.
Khatter, H., et al., 2014. Purification, characterization and crystallization of the human 80S ribosome. Nucleic Acids Res. 42, e49.
Khatter, H., Myasnikov, A.G., Natchiar, S.K., Klaholz, B.P., 2015. Structure of the human 80S ribosome. Nature 520, 640–645.
Klaholz, B.P., 2015. Structure Sorting of Multiple Macromolecular States in Heterogeneous Cryo-EM Samples by 3D Multivariate Statistical Analysis. Open J. Stat. 05, 820.
Klaholz, B.P., 2019. Deriving and refining atomic models in crystallography and cryo-EM: the latest Phenix tools to facilitate structure analysis. Acta Crystallogr. Sect. Struct. Biol. 75, 878–881.
Klaholz, B.P., Myasnikov, A.G., van Heel, M., 2004. Visualization of release factor 3 on the ribosome during termination of protein synthesis. Nature 427, 862–865.
Köhler, A., 1893. Ein neues Beleuchtungsverfahren für mikrophotographische Zwecke. 10, 433–440. Z. Für Wiss. Mikrosk. Für Mikrosk.Tech.
Kucukelbir, A., Sigworth, F.J., Tagare, H.D., 2014. Quantifying the local resolution of cryo-EM density maps. Nat. Methods 11, 63–65.
Lepault, J., Booy, F.P., Dubochet, J., 1983. Electron microscopy of frozen biological suspensions. J. Microsc. 129, 89–102.
Liebschner, D., et al., 2019. Macromolecular structure determination using X-rays, neutrons and electrons: recent developments in Phenix. Acta Crystallogr. Sect. Struct. Biol. 75, 861–877.
Maki-Yonekura, S., Hamaguchi, T., Naitow, H., Takaba, K., Yonekura, K., 2021. Advances in cryo-EM and ED with a cold-field emission beam and energy filtration -Refinements of the CRYO ARM 300 system in RIKEN SPring-8 center. Microsc. Oxf. Engl. 70, 232–240. https://doi.org/10.1093/jmicro/dfaa052.
Mastronarde, D.N., 2003. SerialEM: A Program for Automated Tilt Series Acquisition on Tecnai Microscopes Using Prediction of Specimen Position. Microsc. Microanal. 9, 1182–1183.
Merk, A., et al., 2020. 1.8 Å resolution structure of β-galactosidase with a 200 kV CRYO ARM electron microscope. IUCrJ 7, 639–643.
Murshudov, G.N., et al., 2011. REFMAC5 for the refinement of macromolecular crystal structures. Acta Crystallogr. D Biol. Crystallogr. 67, 355–367.
Myasnikov, A.G., et al., 2016. Structure-function insights reveal the human ribosome as a cancer target for antibiotics. Nat. Commun. 7, 12856.
Nakane, T., et al., 2020. Single-particle cryo-EM at atomic resolution. Nature 587, 152–156.
Nakane, T., Kimanius, D., Lindahl, E., Scheres, S.H., 2018. Characterisation of molecular motions in cryo-EM single-particle data by multi-body refinement in RELION. eLife 7, e36861.
Natchiar, S.K., Myasnikov, A.G., Kratzat, H., Hazemann, I., Klaholz, B.P., 2017. Visualization of chemical modifications in the human 80S ribosome structure. Nature 551, 472–477.
Penczek, P.A., Frank, J., Spahn, C.M.T., 2006. A method of focused classification, based on the bootstrap 3D variance analysis, and its application to EF-G-dependent translocation. J. Struct. Biol. 154, 184–194.
Pettersen, E.F., et al., 2004. UCSF Chimera–a visualization system for exploratory research and analysis. J. Comput. Chem. 25, 1605–1612.
Pettersen, E.F., et al., 2021. UCSF ChimeraX: Structure visualization for researchers, educators, and developers. Protein Sci. Publ. Protein Soc. 30, 70–82.
Rosenthal, P.B., Henderson, R., 2003. Optimal determination of particle orientation, absolute hand, and contrast loss in single-particle electron cryomicroscopy. J. Mol. Biol. 333, 721–745.
Scheres, S.H.W., et al., 2007. Disentangling conformational states of macromolecules in 3D-EM through likelihood optimization. Nat. Methods 4, 27–29.
Simonetti, A., et al., 2008. Structure of the 30S translation initiation complex. Nature 455, 416–420.
Smart, O.S., et al., 2012. Exploiting structure similarity in refinement: automated NCS and target-structure restraints in BUSTER. Acta Crystallogr. D Biol. Crystallogr. 68, 368–380.
Sun, M., et al., 2021. Practical considerations for using K3 cameras in CDS mode for high-resolution and high-throughput single particle cryo-EM. J. Struct. Biol. 213, 107745.
van Heel, M., Schatz, M., 2005. Fourier shell correlation threshold criteria. J. Struct. Biol. 151, 250–262.
von Loeffelholz, O., et al., 2017. Focused classification and refinement in high-resolution cryo-EM structural analysis of ribosome complexes. Curr. Opin. Struct. Biol. 46, 140–148.
von Loeffelholz, O., et al., 2018. Volta phase plate data collection facilitates image processing and cryo-EM structure determination. J. Struct. Biol. 202, 191–199.
von Loeffelholz, O., Klaholz, B.P., 2021. Setup and troubleshooting of Volta phase plate cryo-EM data collection. In: Molecular Biology - Structural Proteomics, 3rd Edition Methods, 2305, pp. 291–299. https://doi.org/10.1007/978-1-0716-1406-8_14.
Wagner, T., et al., 2019. SPHIRE-crYOLO is a fast and accurate fully automated particle picker for cryo-EM. Commun. Biol. 2.
Wang, J., Natchiar, S.K., Moore, P., Klaholz, B., 2021. Identification of Mg 2+ ions next to nucleotides in cryo-EM maps using electrostatic potential maps. Acta Crystallogr. Sect. Struct. Biol. 77, 534.
Weis, F., Hagen, W.J.H., 2020. Combining high throughput and high quality for cryo-electron microscopy data collection. Acta Crystallogr. Sect. Struct. Biol. 76, 724–728.
White, H.E., Saibil, H.R., Ignatiou, A., Orlova, E.V., 2004. Recognition and separation of single particles with size variation by statistical analysis of their images. J. Mol. Biol. 336, 453–460.
Wu, M., Lander, G.C., Herzik, M.A., 2020. Sub-2 Angstrom resolution structure determination using single-particle cryo-EM at 200 keV. J. Struct. Biol. X 4, 100020.
Yip, K.M., Fischer, N., Paknia, E., Chari, A., Stark, H., 2020. Atomic-resolution protein structure determination by cryo-EM. Nature 587, 157–161.
Zhang, K., 2016. Gctf: Real-time CTF determination and correction. J. Struct. Biol. 193, 1–12.
Zhang, X., et al., 2021. Evolving cryo-EM structural approaches for GPCR drug discovery. Struct. Lond. Engl. 1993 (29), 963–974.e6.
Zhang, K., Pintilie, G.D., Li, S., Schmid, M.F., Chiu, W., 2020. Resolving individual atoms of protein complex by cryo-electron microscopy. Cell Res. 30, 1136–1139.
Zivanov, J., et al., 2018. New tools for automated high-resolution cryo-EM structure determination in RELION-3. eLife 7, e42166.
Zivanov, J., Nakane, T., Scheres, S.H.W., 2020. Estimation of high-order aberrations and anisotropic magnification from cryo-EM data sets in RELION-3.1. IUCrJ 7, 253–267.